A&A 421, 1087–1099 (2004)
DOI: 10.1051/0004-6361:20035752

Astronomy & Astrophysics

The relationship of CO abundance to extinction and $N(H_2)$:

Observations of globules and the dependence on star formation activity⋆,⋆⋆

P. Harjunpää[1,2], K. Lehtinen[2], and L. K. Haikala[3]

[1] Institute of Astronomy, ETH Zentrum, 8092 Zürich, Switzerland
[2] Observatory, PO Box 14, 00014 University of Helsinki, Finland
[3] Swedish-ESO Submillimetre Telescope, European Southern Observatory, Casilla 19001, Santiago, Chile

Received 26 November 2003 / Accepted 6 April 2004

Abstract. We have studied the ratio of ^{13}CO and C^{18}O column densities to the extinction A_J of background field stars in the direction of three globules: B 133, B 335, L 466. Selected positions in the globules were observed in the ^{12}CO($J = 1 - 0$) line and in $J = 1 - 0$ and $J = 2 - 1$ transitions of ^{13}CO and C^{18}O using the 15-m Swedish-ESO Submillimetre Telescope (SEST) in Chile. One of the clouds, L 466, was also mapped in the C^{18}O($J = 1 - 0$) line. In addition to the $N(^{13}CO)/A_J$ and $N(C^{18}O)/A_J$ ratios also the ratios of $N(^{13}CO)$ and $N(C^{18}O)$ to A_V and $N(H_2)$ are given. These ratios were found to vary from cloud to cloud so that they are larger in B 335 than in B 133 and L 466. These variations are thought to primarily arise from variations of the column density ratio of CO and its isotopes to H_2. The alternative explanation in terms of the $N(H_2)/A_J$ ratio being larger in starforming regions (B 335) than in more quiescent regions lacking star formation (B 133 and L 466) appears less likely. We also discuss the evidence for $N(CO)/A_J$ variations on the basis of previous observations in star forming and non-star forming dark clouds.

Key words. ISM: general – ISM: abundances – ISM: molecules

1. Introduction

Since the main constituent of interstellar molecular clouds, molecular hydrogen (H_2), is generally unobservable with direct measurements it is common to use carbon monoxide (CO), the second most abundant molecule in the interstellar medium, and its isotopes as tracers of H_2. It is usual to measure the distribution and mass of H_2 in molecular clouds using one canonical $N(H_2)$ to $N(CO)$ ratio (see e.g., Sanders et al. 1984), where CO here stands for the different isotopes of CO, such as ^{13}CO and/or C^{18}O. However, there is no theoretical reason why there should be one universal $N(H_2)/N(CO)$ ratio for molecular clouds, even though in most chemical schemes the presence of H_2 is important for effective production of CO (Williams 1985). Instead, according to Williams, the ratio may vary from cloud to cloud and even within a cloud. The abundance of gas-phase CO in molecular clouds is decreased by collisions between CO molecules and cold dust grains. In these collisions CO sticks to grains forming solid molecular mantles on their surfaces. In regions with high star forming activity the depletion of CO is decreased by removal of molecular mantles from grain surfaces (cf. Charnley et al. 1988). According to this model the abundance of gas-phase CO should correlate with the local level of star forming activity. Therefore in the studies of interstellar clouds and their evolution, the ratio $N(CO)/N(H_2)$ and its variations are of crucial importance.

The $N(CO)/A_V$ ratio and the CO/H_2 abundance ratio have been determined in several earlier studies, beginning with the research of Encrenaz et al. (1975). One way to approach this problem is to estimate the column density of molecular hydrogen from the visual extinction which is derived from star count measurements (e.g., Dickman 1978). The same goal was reached by Frerking et al. (1982, hereafter FLW) for Taurus and ρ Oph clouds by using extinctions derived from near-infrared colour excesses of background stars. A third method based both on colour excesses and star counts in the near-infrared waveband was presented by Lada et al. (1994).

The present paper is the second one in the series in which our purpose is to study the ratio of $N(^{13}CO)$ and $N(C^{18}O)$ to near-infrared extinction in the local interstellar medium. In the first paper (Harjunpää & Mattila 1996, hereafter Paper I) we had chosen three local molecular clouds: the two active star forming regions Cha I and R CrA and a quiescent globule in the Coalsack. In Paper I, we found evidence that the

Send offprint requests to: P. Harjunpää,
e-mail: paivi.harjunpaa@helsinki.fi

⋆ Appendix A is only available in electronic form at the CDS via anonymous ftp to cdsarc.u-strasbg.fr (130.79.128.5) or via http://cdsweb.u-strasbg.fr/cgi-bin/qcat?J/A+A/421/1087

⋆⋆ Appendices B and C are only available in electronic form at http://www.edpsciences.org

$N(^{13}CO)/E(J-K)$ and $N(C^{18}O)/E(J-K)$ ratios are affected by the star forming activity of the cloud so that the higher the activity in the region, the higher these ratios tend to be. However, the only non-star-forming cloud in our sample was a globule in the Coalsack, clearly a different type of cloud from the other clouds in the sample. Therefore, one of our aims in the present study is to confirm if the variations of the $N(^{13}CO)$ and $N(C^{18}O)$ to extinction ratios for isolated globules agree with the trend found in Paper I, or if these ratios in globules are actually different from the values for other dark clouds.

For the present study of the $N(^{13}CO)/A_J$ and $N(C^{18}O)/A_J$ ratios (and finally also the ratios of $N(^{13}CO)$ and $N(C^{18}O)$ to A_V and $N(H_2)$), as well as the reasons for their variations in globules, we have chosen three globules: B 335, B 133 and L 466. B 335 was chosen because it is a representative of dense globules with an embedded protostar. B 133 and L 466 were selected for this study as non-star-forming globules. B 133 was regarded as non-star-forming by Klebe & Jones (1990). Yun & Clemens (1990) found, however, an IRAS source which might be related to the globule B 133 (known also as CB 180) (Yun 1997). However the identification of the young stellar object (YSO) in this particular case was less certain than for other more evident cases (Yun & Clemens 1994, 1995). In L 466 (also known as CB 132) Yun & Clemens (1990) did not find any YSO candidates (Yun 1997). In the present work, we have classified the clouds as "star-forming" or "non-star-forming", simply on the basis of the association to YSOs. As star-forming clouds, we have considered those clouds with at least one associated YSO whereas we considered as quiescent clouds those without any known YSO. Lines of sight in the direction of these globules were selected for this study in the same way as in Paper I, choosing background stars for which there were near-infrared photometry data available from the literature at the time of the beginning of this project.

The Two Micron All-Sky Survey (2MASS) near-infrared photometry of stars in the direction of these globules was used to derive the A_J extinction values. Combined with our CO observations these data permit us to study the $N(^{13}CO)/A_J$ and $N(C^{18}O)/A_J$ ratios in different types of globules, ranging from quiescent to those harbouring active star formation.

2. CO observations

The CO observations were made in three separate runs with the Swedish-ESO Submillimetre Telescope (SEST) in October 1993, April 1994 and August 1998. The observed positions are listed in Table 1 and are shown projected on the extinction maps (Figs. 1–3). These positions were observed in the $^{12}CO(J=1-0)$ line and in $J=1-0$ and $J=2-1$ transitions of ^{13}CO and $C^{18}O$. The half-power beamwidth of the telescope at the frequencies of the $CO(J=1-0)$ and $CO(J=2-1)$ lines is 45″ and 23″, respectively. The receivers for the observations of $J=1-0$ transition were a cooled 3 mm Schottky mixer (Booth et al. 1989) and an IRAM 3 mm SIS receiver, while the observations of the $J=2-1$ transition were made with an IRAM 1 mm SIS receiver. The system temperature (T_{sys}) for $^{12}CO(J=1-0)$ transition ranges from 400 to 700 K, while for ^{13}CO and $C^{18}O$ $J=1-0$ and $J=2-1$ transitions it was around 250 K and 300 K, respectively. Typical observation times for ^{12}CO, ^{13}CO and $C^{18}O$ lines were 2, 5 and 15 min, respectively. This resulted in signal-to-noise ratios better than 20, 50, 5, 10 and 4 at the frequencies of $^{12}CO(J=1-0)$, $^{13}CO(J=1-0)$, $C^{18}O(J=1-0)$, $^{13}CO(J=2-1)$ and $C^{18}O(J=2-1)$, respectively. In addition to these observations, L466 was mapped in $C^{18}O(J=1-0)$ line with the SEST-telescope in October 1996 over 220 positions in a regular 40″ grid. Integration time of 60 s per position was used. The

Table 1. Positions observed with SEST and the *J* band extinctions.

Position	RA (1950)			Dec (1950)			A_J	$\pm\Delta A_J$
	(h)	(m)	(s)	(°)	(′)	(″)	(mag)	(mag)
B 335								
A4	19	34	25.3	7	28	17	0.94	0.13
A5	19	34	27.6	7	27	17	0.57	0.12
A6	19	34	30.2	7	28	29	1.49	0.17
A7	19	34	31.3	7	27	17	1.75	0.15
A8	19	34	32.8	7	26	5	1.23	0.13
A9	19	34	41.4	7	26	5	0.44	0.13
A10	19	34	42.6	7	29	11	0.58	0.13
A11	19	34	44.9	7	27	17	0.29	0.18
A12	19	34	34.0	7	27	0	3.57	0.26
A13	19	34	34.0	7	28	0	3.28	0.25
A14	19	34	38.0	7	27	0	1.08	0.17
B 133								
B2	19	3	28.4	−6	59	15	2.45	0.12
B3	19	3	28.7	−6	56	53	3.86	0.32
B4	19	3	29.2	−6	58	33	4.90	0.22
B5	19	3	29.8	−6	55	55	1.17	0.16
B6	19	3	30.1	−7	0	31	0.47	0.12
B7	19	3	33.3	−6	59	33	1.78	0.13
B8	19	3	34.8	−6	56	49	1.96	0.15
B9	19	3	35.2	−6	58	17	5.42	0.22
B10	19	3	35.4	−6	58	35	4.01	0.21
B11	19	3	37.9	−7	0	31	0.73	0.10
B12	19	3	39.9	−6	59	56	1.48	0.12
B13	19	3	40.2	−6	58	36	2.30	0.15
B14	19	3	40.5	−6	57	32	1.73	0.12
L 466								
C1	18	16	55.0	−6	8	30	0.54	0.11
C3	18	16	57.5	−6	5	30	0.63	0.10
C4	18	16	58.9	−6	7	0	1.10	0.09
C6	18	17	0.8	−6	8	15	1.43	0.12
C9	18	17	3.0	−6	7	0	1.97	0.14
C13	18	17	9.7	−6	5	7	0.85	0.11
C14	18	17	9.8	−6	9	45	0.93	0.11
C15	18	17	10.2	−6	4	7	0.65	0.11
C18	18	17	18.1	−6	5	45	0.89	0.08
C19	18	17	18.5	−6	7	0	0.93	0.10
C20	18	17	21.6	−6	4	30	0.49	0.09

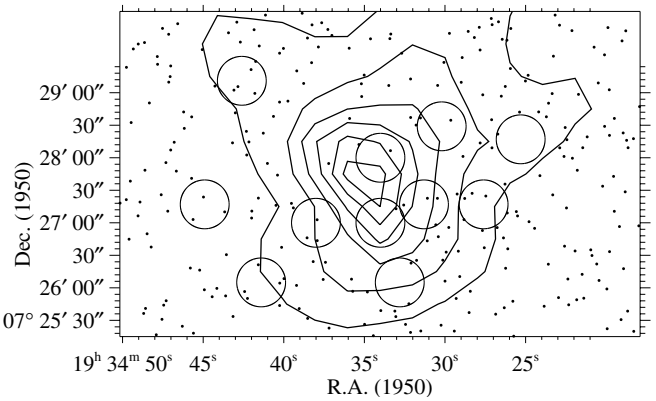

Fig. 1. Extinction map derived from the 2MASS data in the direction of B 335. A_J contours are ranging from 0.5 to 3.0 mag in steps of 0.5 mag. The location of the stars found from the 2MASS archive for the extinction determination are shown with dots. The open circles indicate the location and size of each CO(1-0) beam.

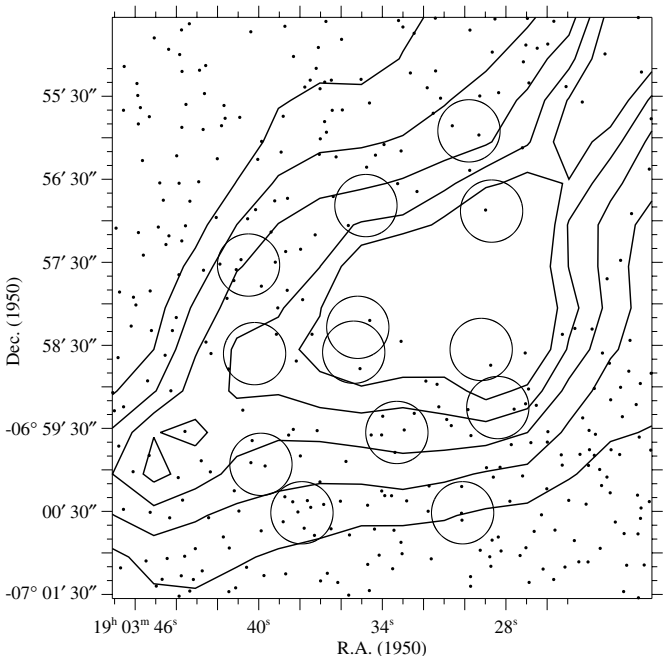

Fig. 2. The same as Fig. 1, but for B 133 and contours are ranging from 0.5 to 2.5 mag in steps of 0.5 mag.

effective T_{sys} was around 200 K. The dense central part of the cloud was further mapped in June 2003 in the same grid over 40 positions using 2 min integration time. The backend was an acousto-optical spectrometer with velocity resolutions of 0.22 and 0.11 km s^{-1} at the frequencies of CO(J = 1−0) and CO(J = 2 − 1), respectively. Calibration was done using the chopper wheel technique. Because of the angular size of these objects, we have chosen to transform antenna temperatures (T_A^*) into radiation temperatures (T_R) by using the mean of the main beam and the Moon efficiency, which is 0.8 and 0.75 at the frequencies of CO(J = 1 − 0) and CO(J = 2 − 1) transitions, respectively. Frequency switching was used for all positions. Pointing was checked using SiO masers and was ∼5 ″.

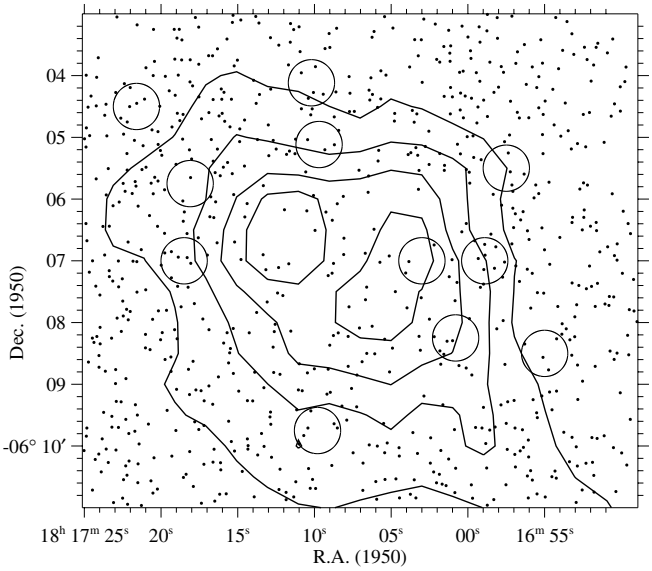

Fig. 3. The same as Fig. 1, but for L 466 and contours are ranging from 0.7 to 1.6 mag in step of 0.3 mag.

3. Extinctions and H_2 column densities

3.1. A_J extinctions

The interstellar extinction curve from visible to ultraviolet wavelengths varies significantly from one line of sight to another. The ratio of total to selective extinction, $R_V = A_V/E(B-V)$, characterizing the mean extinction law, appears to have typically larger values in dark than in diffuse clouds (Cardelli et al. 1989). However, for $\lambda > 0.7$ μm the various extinction curves (i.e. diffuse or dark cloud dust) seem to be practically universal (cf. Clayton & Mathis 1988). Consequently, it is better to use an infrared extinction, e.g. A_J, as dust column density indicator instead of the commonly used $E(B-V)$. The choice of A_J is especially practical in the current study, since we intend to examine dark clouds and their high-extinction cores, where optical extinctions cannot be measured.

Our present study is mainly based on the near-infrared extinction A_J. In order to derive near-IR extinctions of stars visible through the clouds we have applied the optimized multi-band technique of Lombardi & Alves (2001), which is a generalization of the color excess method using data in two bands only. This method combines brightness measurements at three near-IR bands for determining the extinction for an individual star. Spatial smoothing is then applied to angularly close stars to obtain the extinction for a particular sky position. Our data comprises J(1.24 μm), H(1.66 μm) and K_s(2.16 μm) band magnitudes from the 2MASS archive.

The intrinsic colors of stars have been determined in extinction-free reference areas located close to the clouds. For the ratio of J band extinction to color excess we have used $A_J/E(J-H) = 2.50$ and $A_J/E(H-K_s) = 4.50$, interpolated from Table 1 of Mathis (1990) at the wavelengths corresponding to the 2MASS survey.

The extinction towards each CO position was derived by using a Gaussian function with $FWHM = 45''$ (same as the beam size of the CO(J = 1 − 0) measurements) as

a weighting function for the individual extinction values. There are two sources of variance of the extinction determinations; variance of the intrinsic colors $(J-H)_0$ and $(H-K)_0$, and variance of the photometry of the field stars. In the A_J map the former source dominates with a 1-σ error $\leq$ 0.25 mag, while the latter source gives typically ~0.04 mag 1-σ error. The resulting A_J values which typically are averages of several stars per beam position, are listed in Table 1.

3.2. Visual extinctions

Also the $N(^{13}CO)/A_V$ and $N(C^{18}O)/A_V$ ratios are derived from our data, since in most studies of the correlation between CO and dust A_V has been used as the dust column density indicator (see e.g., Dickman 1978; Bachiller & Cernicharo 1986). This is so despite the fact that a near-infrared extinction, e.g. A_J, would be more appropriate since it is independent of the value of R_V.

We have estimated the visual extinctions from the A_J values by adopting for the ratio A_V/A_J the value of 3.31. This value is the mean of the two extremes, 3.55 and 3.06, which are given by Mathis (1990, Table 1) for the "diffuse dust" and the "outer-cloud dust", respectively. This choice of A_V/A_J causes an uncertainty in the A_V-values but is only ~±8%. The chosen value of A_V/A_J and its uncertainty should reflect the average situation and the real variations of R_V found in interstellar clouds. The corresponding value of R_V for this choice of A_V/A_J is 4.0.

3.3. H_2 column densities

We have estimated the H_2 column densities along the observed lines of sight from the adopted extinction A_J values. For this purpose we needed to find a value for the $N(H_2)/A_J$ ratio. As a starting point, we chose to use the value 5.8×10^{21} cm^{-2} mag^{-1} for the $N(H+2H_2)/E(B-V)$ ratio, as determined for diffuse clouds (Bohlin et al. 1978). As a second step we adopt for the $A_J/E(B-V)$ ratio the value 0.87 (Mathis 1990, "diffuse dust"). This combination gives us $N(H+2H_2)/A_J = 6.67\times10^{21}$ cm^{-2} mag^{-1}. It seems logical to adopt this value of the $N(H+2H_2)/A_J$ ratio as a first approximation for both diffuse and dense clouds of the local interstellar medium, since the extinction curves for both cloud types at $\lambda > 0.7$ μm are similar. Finally, if we make the frequently used assumption that all hydrogen in dense clouds is in molecular form we end up with the relation:

$$\frac{N(H_2)}{A_J} = 3.3\times10^{21} \text{ molecules cm}^{-2} \text{ mag}^{-1}. \quad (1)$$

Vuong et al. (2003) have used X-ray absorption to study the $N(H,X)/A_J$ ratio in nearby dense clouds, particularly in the direction of ρ Oph. They found that the $N(H)/A_J$ ratio in ρ Oph is in agreement with the galactic $N(H)$ vs. A_J correlations and they did not find any correlation between the deviations of the $N(H)/A_J$ ratio and the column density. Thus their results give support for using the same $N(H)/A_J$ ratio also for dense clouds.

4. CO column densities

We have estimated ^{13}CO and $C^{18}O$ column densities with two slightly different models. Firstly with the traditional LTE model. However, this method gave incompatible results from the data of $J = 1-0$ and $J = 2-1$ transitions. Therefore we developed another, somewhat modified model in which the excitation temperature of higher rotational transitions is allowed to differ from the $T_{ex}(J = 1-0)$. These methods are described in more detail in the following chapters. The line parameters for $J = 1-0$ and $J = 2-1$ transitions are given in Appendix A which is accessible in electronic form.

4.1. The standard LTE approximation

We have chosen to calculate the so-called LTE column densities, $N_{LTE}(^{13}CO)$ and $N_{LTE}(C^{18}O)$, in order to determine values which are comparable with the column densities obtained from the commonly preferred method. LTE calculations of $N_{LTE}(^{13}CO)$ and $N_{LTE}(C^{18}O)$ are based on the following assumptions: (1) the excitation temperature can be obtained using the ^{12}CO line temperature; (2) the same T_{ex} is valid for the ^{13}CO and $C^{18}O$ isotopes and (3) T_{ex} gives correct populations for higher rotational levels; and (4) the excitation temperature is uniform along the line of sight. Thus, this method gives rough estimates rather than true column densities.

Excitation temperatures were obtained from the $^{12}CO(J = 1-0)$ line by assuming the line to be optically thick ($\tau \gg 1$) and using the equation:

$$T_R = \left[J(T_{ex}) - J\left(T_{bg}\right)\right](1 - e^{-\tau}), \quad (2)$$

where $T_{bg} = 2.7$ K and the function $J(T)$ is defined by

$$J(T) = \frac{T_o}{\exp(T_o/T) - 1}, \quad (3)$$

where $T_o = h\nu/k$ and ν is the frequency of the line. These give for T_{ex} the equation:

$$T_{ex} = \frac{T_o}{\log\left[1 + \frac{T_o}{T_R + J(T_{bg})}\right]}. \quad (4)$$

This T_{ex} was then used for determining optical thicknesses of $^{13}CO(J = 1-0)$ and $C^{18}O(J = 1-0)$ lines:

$$\tau = \log\left[\frac{J(T_{ex}) - J\left(T_{bg}\right)}{J(T_{ex}) - J\left(T_{bg}\right) - T_R}\right]. \quad (5)$$

We derived τ_{ch} in each channel of a line for the $J = 1-0$ transition of ^{13}CO and $C^{18}O$ molecules. The excitation temperature was assumed to be the same for all channels of a spectrum. The next step was to calculate the ground state column densities (N_o) of CO isotopes from the observations of $J = 1-0$ transitions using the equation:

$$N_o = 6.62\times10^{14}\frac{\sum\tau_{ch}\Delta v}{1 - e^{\frac{-T_o(1-0)}{T_{ex}}}} \text{ cm}^{-2}, \quad (6)$$

where Δv is the channel width in km s^{-1}. Finally an estimate for the total column density ($N_{\rm LTE}$) was reached by multiplying $N_{\rm o}$ by the partition function:

$$N_{\rm LTE} = N_{\rm o} \times \sum_{J=0}^{J_{\rm max}} (2J+1) \exp\left[\frac{-h\nu_{10}J(J+1)}{2kT_{\rm ex}}\right]. \quad (7)$$

The uncertainty of a given column density is estimated by taking into account statistical errors and a 10% calibration uncertainty. The resulting column density estimates calculated from $J = 1-0$ transition data for ^{13}CO and C^{18}O are given in Appendix B which is available in electronic form.

We also calculated the column densities using the $J = 2-1$ spectra. The procedure and equations are the same as in the case of $J = 1-0$ transitions, even incorporating the same $T_{\rm ex}$ in accordance with LTE assumptions. The only difference is that instead of Eq. (6), calculation of the column density in the ground state is as follows:

$$N_{\rm o} = 3.19 \times 10^{14} \frac{e^{T_{\rm o}(1-0)/T_{\rm ex}}}{1 - e^{-T_{\rm o}(2-1)/T_{\rm ex}}} \sum \tau_{\rm ch} \Delta v \ {\rm cm}^{-2}. \quad (8)$$

The observations of $J = 2-1$ transitions were originally chosen in order to achieve better angular resolution in these rather small molecular clouds, and also to obtain an independent estimate of the excitation temperature. By assuming the traditional LTE approximation, the calculations based on the $J = 2-1$ data produced significantly lower total column densities than the $J = 1-0$ data. One cause for this could be saturation of the $J = 2-1$ line. However, by looking at the line profiles and the line ratios in different parts of the clouds this appears unlikely. Thus the most probable reason for the discrepancy is that the excitation temperature of the rotational transition $J = 2-1$ is lower than expected on the basis of LTE, i.e. the excitation is subthermal.

4.2. A model allowing different excitation temperatures for higher rotational transitions

In order to approach the possibility of the $J = 2-1$ transitions of CO isotopes being subthermally excited, we have chosen to assume that both the $J = 1-0$ and $J = 2-1$ transitions should give the same total column densities despite the fact that beam sizes are not the same at these two frequencies. This method should therefore yield a mean column density for the two sizes of beams.

A first estimate of the excitation temperature of the rotational transition $J = 2-1$ may be obtained by assuming that there is no need for additional beam filling corrections and that the excitation temperature of the $J = 1-0$ transition is given by the ^{12}CO($J = 1-0$) line using the assumption of an optically thick line and Eq. (4). A single $T_{\rm ex}(J = 2-1)$ value for all the channels of a line was then obtained by iterating on

$$2\frac{\sum \tau_{\rm ch}(1-0)\Delta v}{\sum \tau_{\rm ch}(2-1)\Delta v} = e^{\frac{-T_{\rm o}(2-1)}{T_{\rm ex}(2-1)}} \times \left[\frac{e^{\frac{-T_{\rm o}(1-0)}{T_{\rm ex}(1-0)}} - 1}{e^{\frac{-T_{\rm o}(2-1)}{T_{\rm ex}(2-1)}} - 1}\right]. \quad (9)$$

This approach was chosen on the basis of the model calculations of Warin et al. (1996). According to them, the rotational population of only the two lowest rotational levels of the three isotopes of CO are usually thermalized in the inner parts of dark clouds. In agreement with this model, the $T_{\rm ex}(J = 2-1)$ values we obtained indicate that the rotational level $J = 2$ of the ^{13}CO and C^{18}O isotopes is subthermally excited. For $T_{\rm ex}(J = 1-0)$ we found values between 9 and 11 K in B 335 and B 133 and 7–8.5 K in L 466. In the case of ^{13}CO $T_{\rm ex}(J = 2-1)$ varies in the range 5.5–7 K in B 335 and B 133 and 4.5–5.5 K in L 466. For C^{18}O the $T_{\rm ex}(J = 2-1)$ values are 0.5–1.5 K lower than for ^{13}CO.

Total column density was then estimated by assuming that the rotational transitions $J = 3-2$ and higher have the same excitation temperature as the $J = 2-1$ transition:

$$\begin{aligned} N &= QN_{\rm o} \\ Q &= 1 + e^{\frac{-T_{\rm o}(1-0)}{T_{\rm ex}(1-0)}} \\ &\quad \times \textstyle\sum_{J=0}^{J_{\rm max}} (2J+1) \exp\left[\left(\frac{-J(J+1)}{2} - 1\right) \times \frac{-T_{\rm o}(1-0)}{T_{\rm ex}(2-1)}\right], \end{aligned} \quad (10)$$

where $N_{\rm o}$ was obtained from Eq. (6). Uncertainties in column densities were estimated using Monte Carlo simulations and by taking into account a 10% calibration uncertainty and the statistical errors. The resulting column densities from this method, $N(^{13}{\rm CO})$ and $N({\rm C}^{18}{\rm O})$, are given in Appendix C and are obtainable in electronic form. Compared to these results, the standard LTE method (based on the data of the $J = 1-0$ transition only) overestimates the total column densities by 10% to 30%.

4.3. Comparison with the column density estimates in Paper I

The method used in Paper I for derivation of column densities differs from the one used here. In Paper I we had observed the emission of CO isotopes in the $J = 1-0$ transitions only, whereas here were able to take advantage of the observations of the $J = 2-1$ transitions as well. In both studies the LTE method gave the highest column densities and the steepest slopes for the $N(^{13}{\rm CO})$ and $N({\rm C}^{18}{\rm O})$ vs. extinction relations. For the globules studied in the present paper, recalculation with the method used in Paper I give ^{13}CO and C^{18}O column densities which differ by 15% at most from the ones obtained with the method described in Sect. 4.2 of the present paper. For most positions, the method used in Paper I gives lower column densities. Adopting the method from Paper I gives, compared to the method presented in Sect. 4.2 of the present paper, flatter slopes for $N(^{13}{\rm CO})$ and $N({\rm C}^{18}{\rm O})$ vs. $A_{\rm J}$ relationships in the direction of B 335 but steeper in the direction of B 133 and L 466.

5. Results

5.1. CO column densities vs. A_J

The column density vs. $A_{\rm J}$ diagrams for $N(^{13}{\rm CO})$ and $N({\rm C}^{18}{\rm O})$ obtained using our method described in Sect. 4.2 and for $N_{\rm LTE}(^{13}{\rm CO})$ and $N_{\rm LTE}({\rm C}^{18}{\rm O})$ obtained assuming LTE conditions are shown in Figs. 4–7, respectively. The error bars in these figures for the column densities are obtained by taking

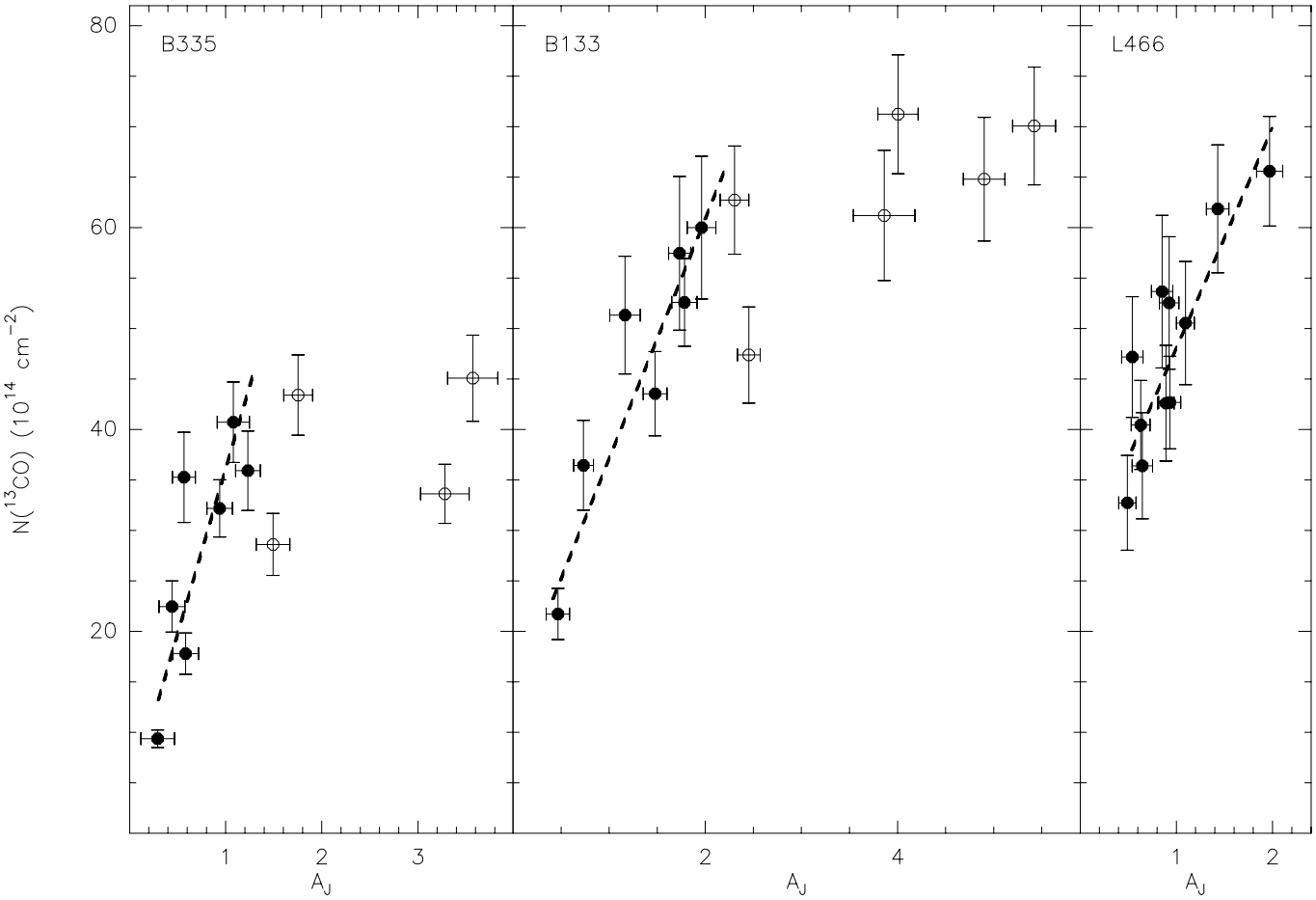

Fig. 4. ^{13}CO column density $N(^{13}CO)$, derived from our model described in Sect. 4.2., as a function of extinction in the direction of B 335, B 133 and L 466. The error bars for column density indicate the statistical errors and a 10% calibration uncertainty. For each cloud, the linear least-squares fit is presented with dashed line and the points omitted from the fit are drawn with open circles.

Table 2. Linear least-squares fit results for $N(^{13}CO)$, $N_{LTE}(^{13}CO)$, $N(C^{18}O)$ and $N_{LTE}(C^{18}O)$ vs. A_J data. The results are presented in the form: $N = (a \pm \Delta a) \times 10^{14}(A_J + (b \pm \Delta b))$ cm^{-2}.

	$N(^{13}CO)$ vs. A_J		$N_{LTE}(^{13}CO)$ vs. A_J		
Cloud	a	b	a	b	A_J
	$\pm\Delta a$	$\pm\Delta b$	$\pm\Delta a$	$\pm\Delta b$	range
B 335	32.7	0.10	42.1	0.07	0.3–1.3
	6.8	0.16	9.0	0.17	
B 133	23.8	0.56	30.1	0.53	0.4–2.2
	3.7	0.19	3.2	0.14	
L 466	21.8	1.20	29.7	0.89	0.5–2.0
	4.5	0.20	3.1	0.10	
	$N(C^{18}O)$ vs. A_J		$N_{LTE}(C^{18}O)$ vs. A_J		
Cloud	a	b	a	b	A_J
	$\pm\Delta a$	$\pm\Delta b$	$\pm\Delta a$	$\pm\Delta b$	range
B 335	4.3	–0.18	5.3	–0.17	0.3–3.6
	0.4	0.09	0.4	0.09	
B 133	2.8	–0.01	3.6	–0.01	0.4–5.5
	0.2	0.10	0.2	0.09	
L 466	6.9	–0.11	7.8	–0.08	0.5–2.0
	0.9	0.11	0.8	0.09	

into account the statistical errors and a 10% calibration uncertainty. In Figs. 6 and 7, we also show with open triangles the column densities obtained from the $J = 2 - 1$ transitions assuming LTE. The ^{13}CO column density increases with A_J in all three globules. In B 335 and B 133, however, there are also signs of high opacity saturating the line at high extinctions. The increase of $C^{18}O$ column density with A_J is plainly visible in all three globules.

We have made linear fits to our $N(^{13}CO)$, $N_{LTE}(^{13}CO)$, $N(C^{18}O)$ and $N_{LTE}(C^{18}O)$ vs. A_J data in each cloud, taking into account the errors in both variables and omitting points likely to be affected by saturation (see Figs. 4 and 6). This was done using Jolivette's (1993) least-squares program. In B 335 and B 133, the ^{13}CO(1-0) emission seems to be saturated, or the effect of depletion has become visible above $A_J \sim 1.3$ and 2.2 mag, respectively, and therefore points corresponding to column densities in the direction of higher extinction than these are omitted from the ^{13}CO fits. In L 466, there are no clear signs of saturation, and therefore all positions are used for the fits. The final results of the least squares fits are presented in Table 2. The resulting fits are also shown as dashed lines in Figs. 4–7. The points omitted from the fits are indicated with open circles.

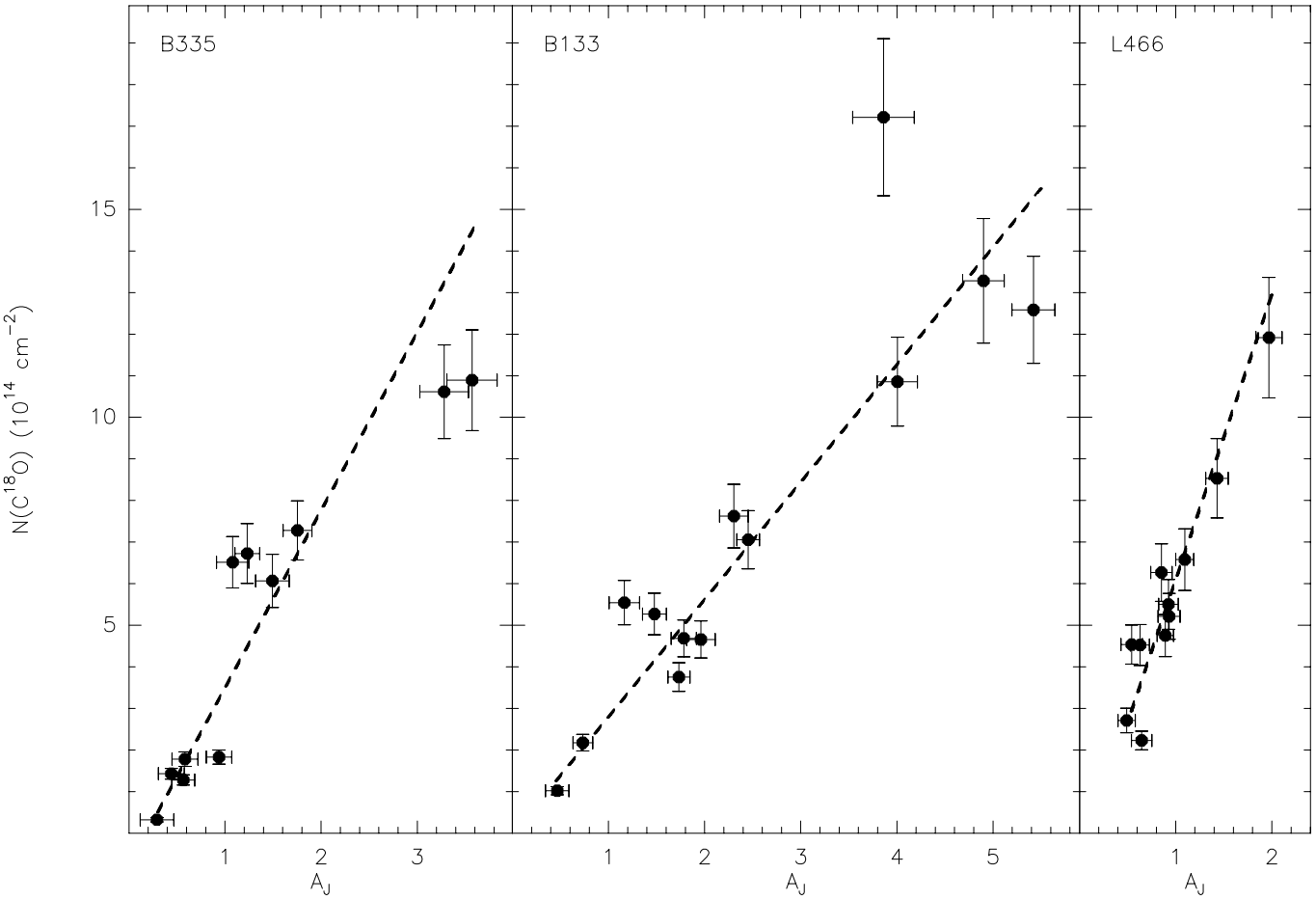

Fig. 5. The same as for Fig. 4, but for $N(C^{18}O)$.

Table 3. Linear least-squares fit results for $N(^{13}CO)$ and $N(C^{18}O)$ vs. A_V data. The results are presented in the form $N = a \times 10^{14}(A_V + b)$ cm^{-2}.

	$N(^{13}CO)$ vs. A_V			$N(C^{18}O)$ vs. A_V		
Cloud	a	b	A_V range	a	b	A_V range
B 335	9.9	0.3	1.0–4.3	1.3	–0.6	1.0–11.9
B 133	7.2	1.9	1.3–7.3	0.9	0.0	1.3–18.2
L 466	6.6	4.0	1.6–6.2	2.1	–0.4	1.6–6.6

5.2. CO column densities vs. A_V

A_J extinctions were transformed into A_V by using the ratio $A_V/A_J = 3.31 \pm 0.25$ as described in Sect. 3.2. The resulting relationships are presented in Table 3.

5.3. CO column densities vs. $N(H_2)$

A_J extinctions have also been converted into H_2 column densities. The transformations have been performed applying an $N(H_2)/A_J$ conversion factor as derived in Sect. 3.3., i.e. 3.3×10^{21} molecules cm^{-2} mag^{-1}. The resulting $N(^{13}CO)$ and $N(C^{18}O)$ vs. $N(H_2)$ relationships are presented in Table 4.

Table 4. The $N(H_2)$ vs. $N(^{13}CO)$ and $N(C^{18}O)$ relationships. The results are presented in the form: $N(CO) = a \times 10^{-7}(N(H_2) + b \times 10^{21})$ cm^{-2}. The unit of $N(H_2)$ ranges is 10^{21} cm^{-2}.

	$N(^{13}CO)$ vs. $N(H_2)$			$N(C^{18}O)$ vs. $N(H_2)$		
Cloud	a	b	$N(H_2)$ range	a	b	$N(H_2)$ range
B 335	9.9	0.3	1.0–4.3	1.3	–0.6	1.0–11.8
B 133	7.2	1.8	1.3–7.3	0.9	0.0	1.3–18.5
L 466	6.6	4.0	1.7–6.6	2.0	–0.4	1.7–6.6

Table 5. Linear least-squares fit results for integrated $J = 1 - 0$ line intensities $I(^{13}CO)$ and $I(C^{18}O)$ vs. $N(H_2)$ data. The results are presented in the form $I = a \times 10^{-22}N(H_2) + b$ cm^{-2}. The unit of $N(H_2)$ ranges is 10^{21} cm^{-2}.

	$I(^{13}CO)$ vs. $N(H_2)$			$I(C^{18}O)$ vs. $N(H_2)$		
Cloud	a	b	$N(H_2)$ range	a	b	$N(H_2)$ range
B 335	7.0	1.0	1.0–4.3	0.9	0.2	1.0–11.8
B 133	6.1	1.6	1.3–7.3	0.8	0.2	1.3–18.5
L 466	3.6	2.9	1.7–6.6	1.7	0.1	1.7–6.6

We also calculated the relationships of the integrated $J = 1 - 0$ line intensities $I(^{13}CO)$ and $I(C^{18}O)$

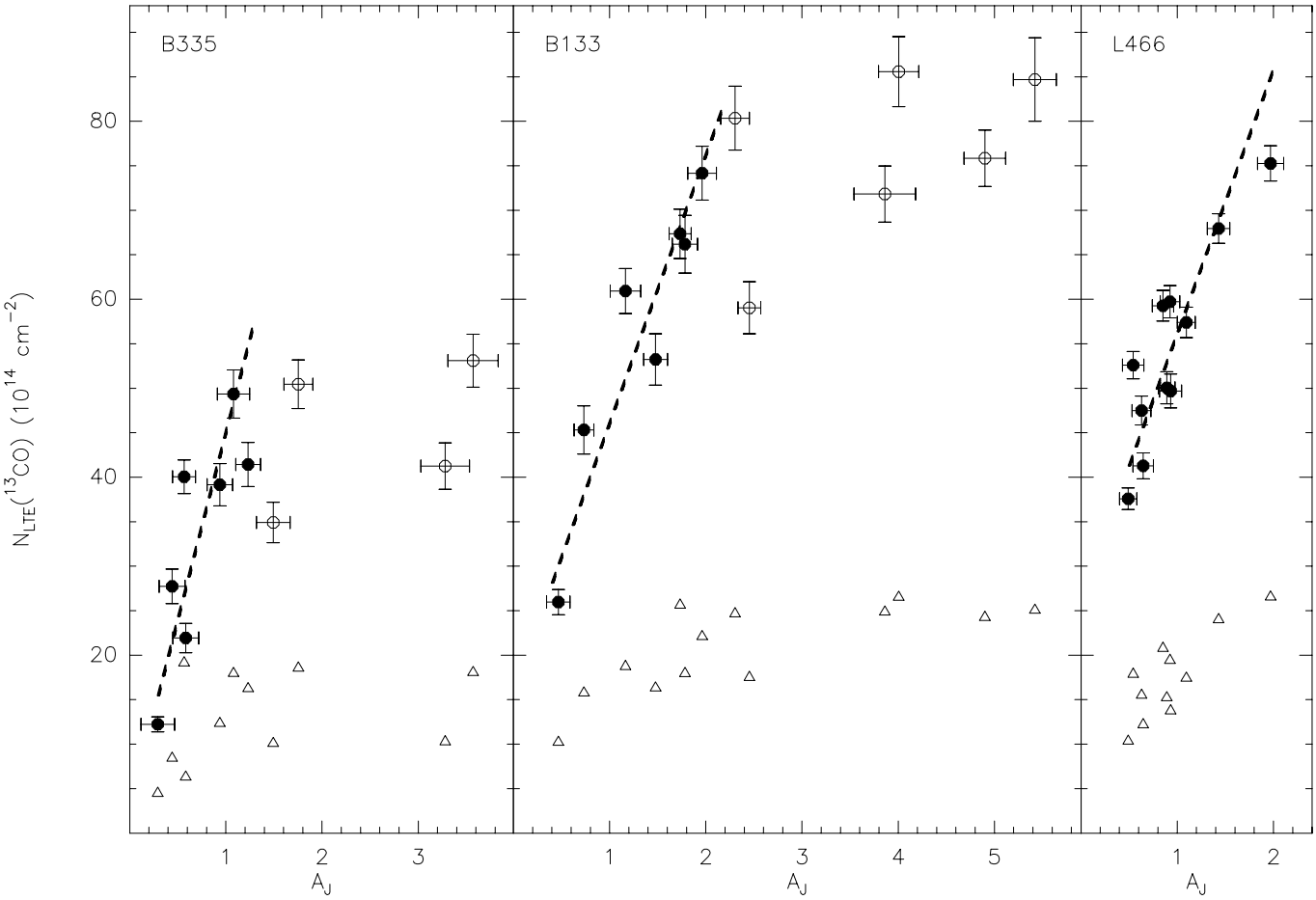

Fig. 6. The same as for Fig. 4, but for $N_{LTE}(^{13}CO)$ derived assuming LTE conditions. In addition, the LTE column densities obtained from the data of $J = 2 - 1$ transition are also shown with open triangles.

to $N(H_2)$. This was again done adopting the value 3.3 × 10^{21} molecules cm^{-2} mag^{-1} for the ratio of $N(H_2)$ and A_J. These results are listed in Table 5.

5.4. $C^{18}O(J = 1 - 0)$ mapping of L 466

The contour map of the integrated area of the $C^{18}O(J = 1 - 0)$ line in L 466 is shown overlaid on a Digitized Sky Survey[1] red image in Fig. 8. A_J contours are indicated with a dashed line in Fig. 8.

[1] The Digitized Sky Survey was produced at the Space Telescope Science Institute under U.S. Government grant NAG W-2166. The images of these surveys are based on photographic data obtained using the Oschin Schmidt Telescope on Palomar Mountain and the UK Schmidt Telescope. The plates were processed into the present compressed digital form with the permission of these institutions. The UK Schmidt Telescope was operated by the Royal Observatory Edinburgh, with funding from the UK Science and Engineering Research Council (later the UK Particle Physics and Astronomy Research Council), until 1988 June, and thereafter by the Anglo-Australian Observatory. The blue plates of the southern Sky Atlas and its Equatorial Extension (together known as the SERC-J), as well as the Equatorial Red (ER), and the Second Epoch [red] Survey (SES) were all taken with the UK Schmidt.

We have calculated the $N_{LTE}(C^{18}O)$ vs. A_J relation also using this mapping. The column densities were estimated using the LTE approximation and assuming the excitation temperature to be 7.5 K over the whole cloud. The resulting $N_{LTE}(C^{18}O)$ vs. A_J diagram is shown in Fig. 9. Making a linear fit to this data set gives the relationship:

$$N_{LTE}(C^{18}O) = 9.95 \times 10^{14}(A_J - 0.12)\ \mathrm{cm}^{-2},$$

which is indicated with a dashed line in Fig. 9. Also the data points of the single positions used in the $N_{LTE}(C^{18}O)$ vs. A_J comparison are shown in Fig. 9 as squares and the fit for this data set is shown with a solid line. The slight difference between these two fits is partially due to the fit based on the mapping being weighted towards lower extinctions. The column density determinations are somewhat more reliable for the single positions since the excitation temperature was estimated for each position separately.

6. Discussion

6.1. $N(CO)/A_J$ vs. star formation activity as derived from the sample of Paper I, this work, and FLW

We have a set of rather homogeneous data available for different kinds of molecular clouds with differing levels of star

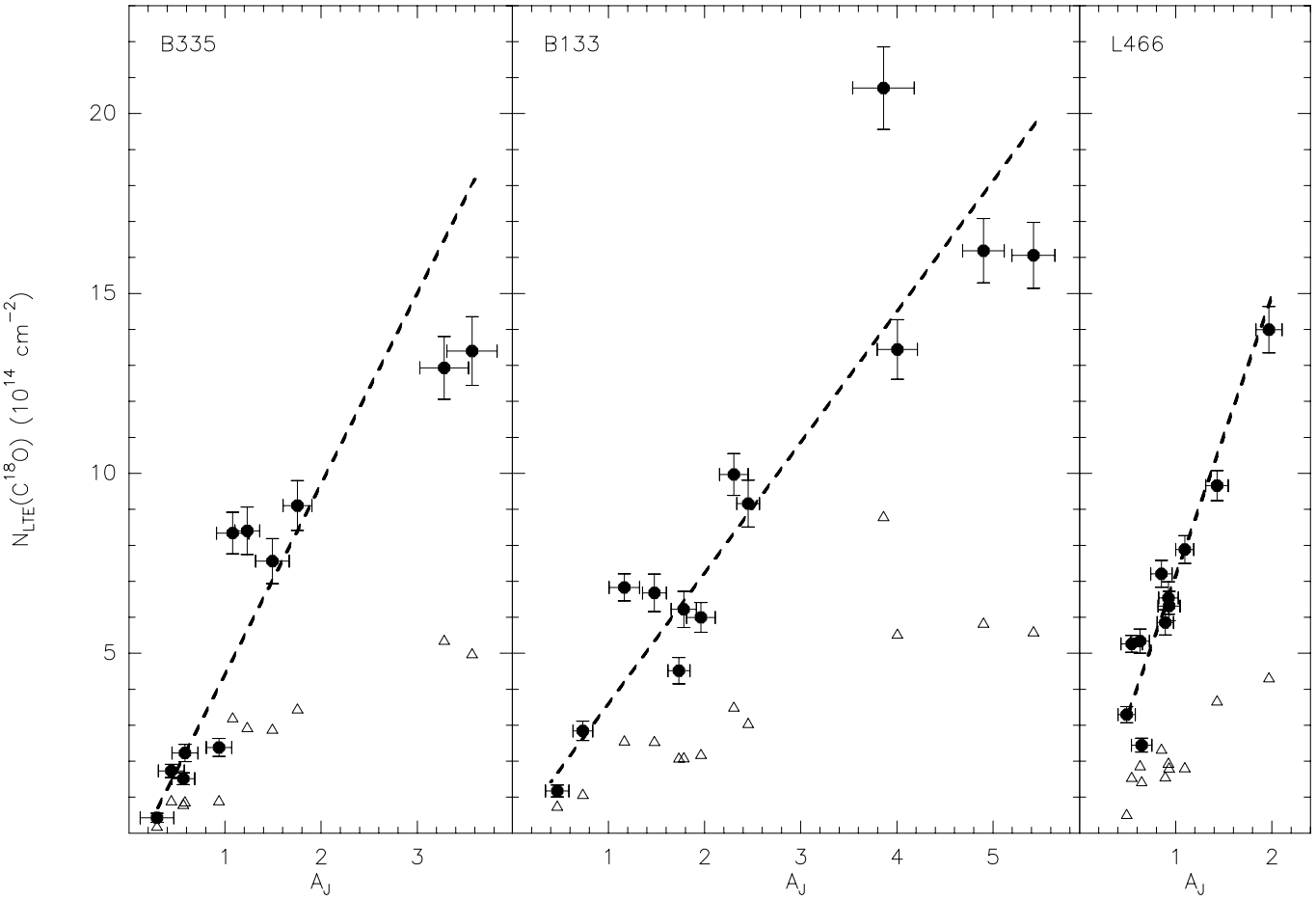

Fig. 7. The same as for Fig. 6, but for $N_{LTE}(C^{18}O)$.

formation activity from FLW, Paper I and the present study. FLW derived the A_V values from the $E(J-K)$ values of Elias (1978a,b). For our comparison we have adopted the original $E(J-K)$ values of Elias (1978a,b) instead of the A_V values, and transformed them to A_J using the ratio $E(J-K)/A_J = 0.62$ (Mathis 1990), which is independent of the value of R_V. In order to have comparable column densities, we have recalculated in Paper I $N_{LTE}(^{13}CO)$ and $N_{LTE}(C^{18}O)$ for ρ Oph and Taurus using the line parameters given by FLW. In the same way, the LTE column densities were obtained from the line parameters as given in Paper I for Cha I, R CrA, and Coalsack and as given in the present paper (in Appendix A) for B 133, B 335 and L 466. The column densities were for this purpose calculated as described in Sect. 4.1., with the exception that the sum $\sum \tau_{ch} \Delta v$ in Eq. (6) was replaced by

$$\frac{\tau}{1-\mathrm{e}^{-\tau}} \times \frac{\int T_R^* \mathrm{d}v}{J(T_{ex}) - J(T_{bg})} \qquad (11)$$

which enables the use of the tabulated integrated line intensity values of FLW. Furthermore, the partition function in Eq. (7) was approximated by $2kT_{ex}/h\nu_{10}$. The resulting fits for these data sets are collected in Table 6 and are also presented graphically in Fig. 10.

The slopes of the relations reflect the fractional abundances of the CO isotopes in each cloud, and the intercepts can be interpreted as extinction thresholds below which the CO isotope in question is not detectable. This type of threshold suggests the presence of a diffuse envelope which is characterized by a larger, strongly dissociative UV radiation field and lower gas density than the main cloud (FLW; Dickman & Herbst 1990). In the sample presented above, the steepness of the $N_{LTE}(^{13}CO)$ vs. A_J slope grows from B 133 to Coalsack, L 466, B 335, Taurus, R CrA, ρ Oph, and finally to Cha I. The slope of the $N_{LTE}(^{13}CO)$ vs. A_J relationship is probably also affected by the chemical fractionation which enhances the abundance of ^{13}CO at low extinctions. In the case of $N_{LTE}(C^{18}O)$ vs. A_J relationships, Cha I has the steepest slope followed by L 466, R CrA, ρ Oph, B 335, Coalsack, B 133, and Taurus.

As discussed in Paper I, the five clouds of FLW and Paper I can be placed in the following order of diminishing star formation activity: Cha I, R CrA, ρ Oph, Taurus, and Coalsack. The chosen order is, however, subjective to some extent. When making this estimate, we have taken into account the kinds of locations within the clouds probed by the observed lines of sight. In Cha I and R CrA, these locations are within regions of strong star forming activity. In ρ Oph, many of them are outside the active centre of star formation. In Taurus, most of the lines of sight are outside the regions of active star formation and the gas they are probing is thus more quiescent overall. In Coalsack, there is no known ongoing star-formation. According to our present knowledge, the globule L 466 is

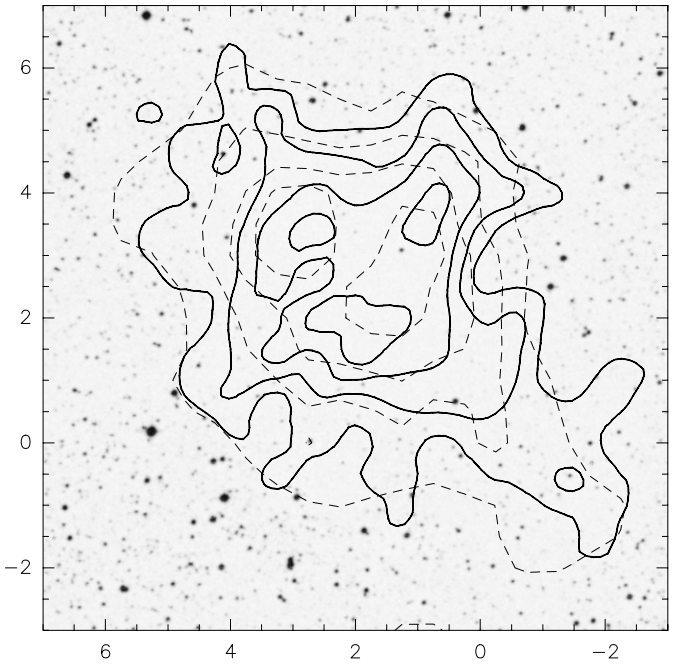

Fig. 8. Map of integrated area of $C^{18}O(J = 1 - 0)$ line (thick solid line) in the units of T_R (K km s^{-1}) overlaid on a DSS red image in the direction of L 466. The (0, 0) position is located at RA $18^h17^m00^s$, Dec $-6°10'00''$ (1950.0).The steps on the coordinate axis are in arc minutes. The velocity range is from 5.26 to 7.83 km s^{-1}. The lowest contour level is 0.6 K km s^{-1} and the highest 1.2 K km s^{-1} and the step is 0.2 K km s^{-1}. The dashed line indicates the A_J contours from Fig. 3.

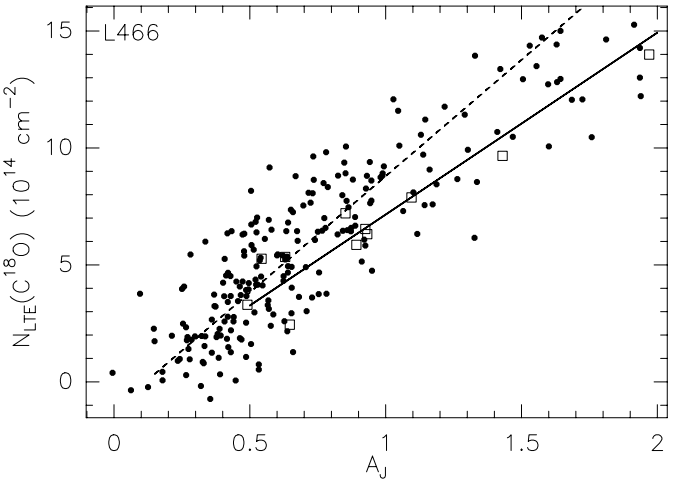

Fig. 9. Column density $N_{LTE}(C^{18}O)$, obtained from $J = 1-0$ mapping, as a function of A_J for the cloud L 466 (dots). The linear least-squares fit is presented with dashed line. Open squares indicate the data points of the individual positions used in the $N(C^{18}O)$ vs. A_J comparison and the fit for this data set is shown with a solid line.

non-star-forming. We have also regarded B 133 here as a globule without star formation, since the YSO detection in the cloud is uncertain (Yun & Clemens 1994, 1995) and there are no clear signs of ongoing star formation. B 335 is a well known example of a small globule with a protostar.

From Table 6 and Fig. 10 one can see that the $N(^{13}CO)$ and $N(C^{18}O)$ vs. A_J correlations considered here vary from cloud to cloud and there seem to be a tendency of these correlations

Table 6. Linear least-squares fit results for $N_{LTE}(^{13}CO)$ and $N_{LTE}(C^{18}O)$ vs. A_J data. The results are presented in the form $N_{LTE}(^{13}CO) = a \times 10^{15}(A_J + b)$ cm^{-2} and $N_{LTE}(C^{18}O) = a \times 10^{14}(A_J + b)$ cm^{-2}.

	$N_{LTE}(^{13}CO)$ vs. A_J		$N_{LTE}(C^{18}O)$ vs. A_J		Ref.
Cloud	a	b	a	b	
ρ Oph	11.5	–0.87	6.4	–1.26	a
Taurus	5.3	–0.42	2.6	0.21	a
Cha I	12.1	–0.83	9.8	–0.78	b
R CrA	6.9	–1.78	6.7	–2.15	b
Coalsack	3.1	–0.32	3.8	–1.44	b
B 335	4.7	0.01	5.2	–0.19	c
B 133	3.0	0.53	3.5	–0.06	c
L 466	3.5	0.67	7.3	–0.10	c
IC 5146	8.4		8.8		d
L 977			7.7	–0.30	e
L 1521B			5.8	2.01	f
L 183			6.7	–0.06	g

a: FLW.
b: Paper I.
c: this work.
d: Lada et al. (1994).
e: Alves et al. (1999).
f: Juvela et al. (1997).
g: Juvela et al. (2002).

to showing steeper slopes in star forming regions than in quiescent clouds. A clear exception to the latter is the $N(C^{18}O)$ vs. A_J relationship in the direction of Taurus. However, as discussed earlier, most lines of sight in this sample do not probe active star forming parts of the cloud. On the other hand, FLW themselves found a clearly higher slope of $N(C^{18}O)/A_J = 6.8 \times 10^{14}$ cm^{-2} mag^{-1} for Taurus sample. This is because they chose to estimate the upper limit of $N(C^{18}O)$ by assuming that $T_{ex}(C^{18}O) = 0.5 \times T_{ex}(^{12}CO)$.

On the basis of the theoretical predictions by Williams (1985) and Charnley et al. (1988) (see Sect. 1), these empirical results can be interpreted as a consequence of differing CO-to-H_2 abundance ratios in the star forming and in the quiescent clouds. These results could, however, also be obtained with a constant CO-to-H_2-ratio if the ratio of $N(H_2)$ and dust column density (measured by e.g. A_J or A_V) varies. However, the results of Vuong et al. (2003) give strong support for a constant ratio $N(H)/A_J$, i.e. the same for diffuse and dense clouds. Alternatively, there is a combination of these two effects. In any case, CO isotopes should not be used uncritically as a precise quantitative tracer of molecular gas in interstellar clouds.

In L 466 the CO, ^{13}CO and $C^{18}O$ lines are broader, and thus the turbulence is larger than in B 335 and B 133 which could cause the steeper than expected slope of $N(C^{18}O)$ vs. A_J relation in this cloud.

6.2. Comparison with other studies of $N(CO)/A_J$

Lada et al. (1994) have determined the distribution of extinction in the molecular cloud complex near the young cluster

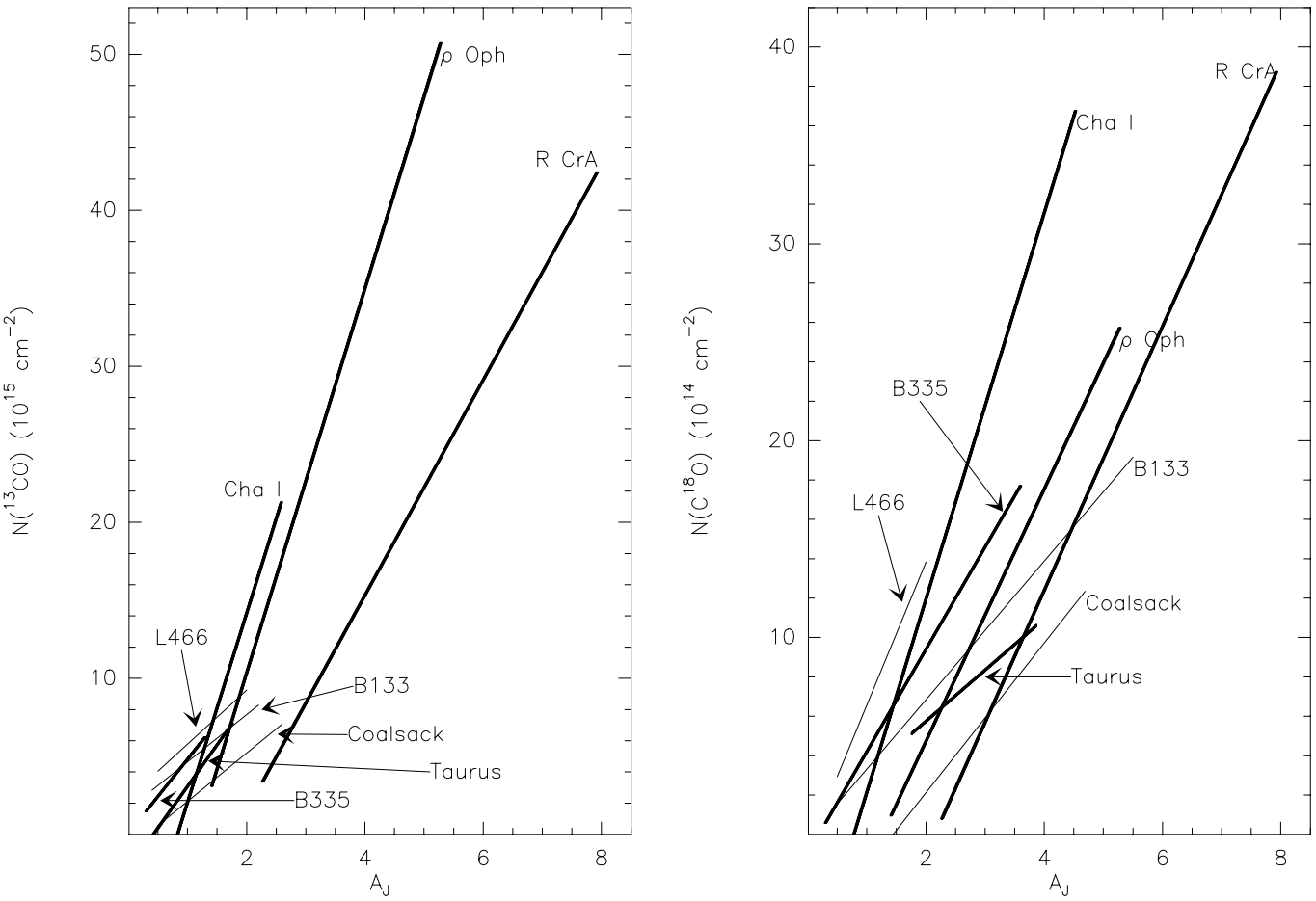

Fig. 10. Graphical presentation of the linear least-squares fits for $N_{\rm LTE}(^{13}{\rm CO})$ and $N_{\rm LTE}({\rm C}^{18}{\rm O})$ vs. $A_{\rm J}$ data. The fits for star forming clouds are drawn with thicker line.

IC 5146. They employed a method based on *JHK* colour excess and star counts. The ^{13}CO and C^{18}O column densities were calculated assuming LTE. In this way, they were able to calculate the ratio of $N_{\rm LTE}(^{13}{\rm CO})$ and $N_{\rm LTE}({\rm C}^{18}{\rm O})$ to extinction in more than 500 locations in the cloud. Even though Lada et al. (1994) originally determined extinction in $E(H-K)$, they preferred to present the results in $A_{\rm V}$. We have therefore transformed the extinctions into $A_{\rm J}$ by using the standard value of 4.13 for the $A_{\rm J}/E(H-K)$ ratio (Mathis 1990). The mean $N_{\rm LTE}(^{13}{\rm CO})$ and $N_{\rm LTE}({\rm C}^{18}{\rm O})$ to $A_{\rm J}$ ratios for IC 5146 found by Lada et al. (1994) can then be presented in the form:

$$\langle N_{\rm LTE}(^{13}{\rm CO})/A_{\rm J}\rangle = 8.4\times10^{15}\ {\rm cm}^{-2}\ {\rm mag}^{-1} \quad (A_{\rm J}\le 1.3\ {\rm mag})$$

and

$$\langle N_{\rm LTE}({\rm C}^{18}{\rm O})/A_{\rm J}\rangle = 8.8\times10^{14}\ {\rm cm}^{-2}\ {\rm mag}^{-1} \quad (A_{\rm J}\le 3.9\ {\rm mag}).$$

Alves et al. (1999) used the method of Lada et al. (1994) for extinction determinations but they improved the spatial compatibility of the extinction and C^{18}O column density maps. After converting $A_{\rm V}$ to $A_{\rm J}$, their result for the non-star forming cloud L 977 can be written in the form:

$$N_{\rm LTE}({\rm C}^{18}{\rm O}) = 7.7\times10^{14}(A_{\rm J}-0.30)\ {\rm cm}^{-2}.$$

Comparing the results obtained by Lada et al. (1994) for IC 5146 with the values shown in the upper part of Table 6, we notice that they match with the values representative of star forming regions. The ratios lie between the values found for R CrA and Cha I. Thus, the results of Lada et al. (1994) provide further support for the idea that the ratio of ^{13}CO and C^{18}O to extinction can be higher in star forming regions than in quiescent clouds. However, the results for L 977 by Alves et al. (1999) give a relatively high value for the $N({\rm C}^{18}{\rm O})$ vs. $A_{\rm J}$ ratio in a non-star forming cloud.

Juvela et al. (1997) have studied the core L 1521B, which belongs to Taurus molecular cloud complex, but has no known current star formation. They gave $N_{\rm LTE}({\rm C}^{18}{\rm O})$ and $E(J-K)$ values for six positions in the cloud. We transformed their $E(J-K)$ values into $A_{\rm J}$ and fitted a straight line to the data using only three positions, for which the positional coincidence of the two data sets is most reliable. This gave the relationship

$$N_{\rm LTE}({\rm C}^{18}{\rm O}) = 5.8\times10^{14}(A_{\rm J}+2.01)\ {\rm cm}^{-2}.$$

Juvela et al. (2002) have also studied a high galactic latitude starless cloud L 183. In the direction of this cloud they found

$$N_{\rm LTE}({\rm C}^{18}{\rm O}) = 6.7\times10^{14}(A_{\rm J}-0.06)\ {\rm cm}^{-2},$$

where we have transformed $A_{\rm V}$ to $A_{\rm J}$ by assuming their ratio to be 3.55. These values of the $N_{\rm LTE}({\rm C}^{18}{\rm O})$ vs. $A_{\rm J}$ slope are

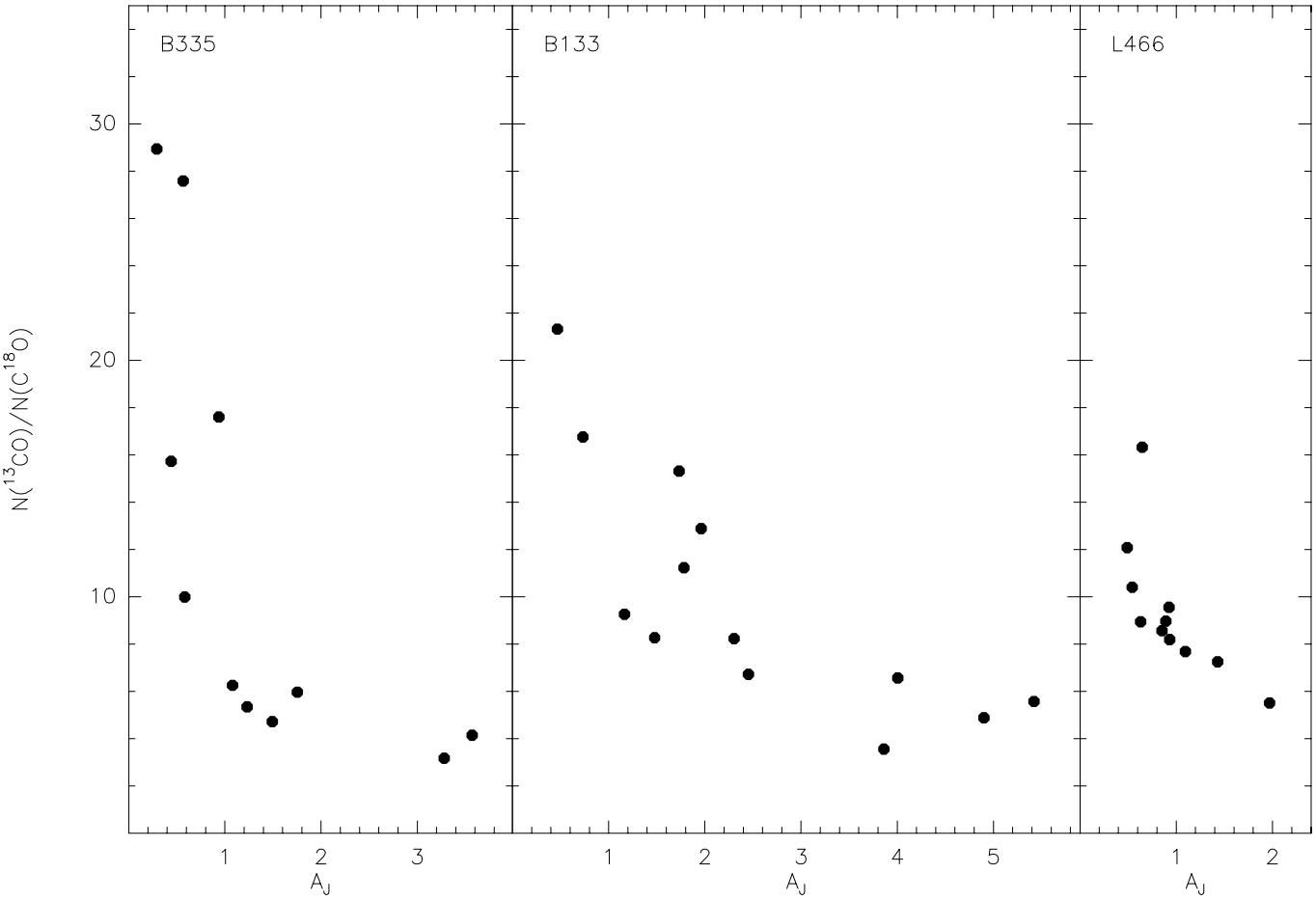

Fig. 11. The ratio $N(^{13}CO)/N(C^{18}O)$ as a function of extinction in the direction of B 335, B 133 and L 466.

intermediate when compared to the results presented in Table 6 and are higher than the values for starless clouds in the upper part of the Table. Hotzel et al. (2002) also concluded that in the starless globule B 68, the fractional abundance of $C^{18}O$ is lower than in star forming regions R CrA, Cha I, and ρ Oph.

Hayakawa et al. (1999, 2001) used the DENIS data to study $N_{LTE}(^{13}CO)$ and $N_{LTE}(C^{18}O)$ vs. A_V relationships in the direction of Cha I–III. They adopted the extinction law of Cardelli et al. (1989), which gives $A_V/A_J = 3.54$. The $N_{LTE}(^{13}CO)$ vs. A_J slope obtained from their results for Cha I is shallower than the one we obtained in Paper I, but their $N_{LTE}(C^{18}O)$ vs. A_V slope was steeper. The lines of sight of our sample are, however, located in their region A, where they found the relationships to be by a factor of ∼2 steeper than the entire cloud average. However, the steepness of the slope they found in region A was suspected to result from underestimates of A_V.

Hayakawa et al. (1999) also summarize the results of previous $N(^{13}CO)$ and $N(C^{18}O)$ vs. A_V studies for many dark clouds by several authors. The slopes vary between 0.7–3.8 × 10^{15} cm^{-2} mag^{-1} for the $N(^{13}CO)$ vs. A_V relationships and between 0.7–3.5 × 10^{14} cm^{-2} mag^{-1} for $N(C^{18}O)$ vs. A_V relationships. Assuming $A_V/A_J = 3.31$ (see Sect. 3.2), the slopes are 2.3–12.6 × 10^{15} cm^{-2} mag^{-1} and 2.3–11.6 × 10^{14} cm^{-2} mag^{-1} for $N(^{13}CO)$ vs. A_J and $N(C^{18}O)$ vs. A_J, respectively. These ranges correspond well to the ones in Table 6.

In addition to our own work, the entire sample presented above is a collection from several works and authors, and is, thus, not a completely uniform and homogeneous sample. However, all of the extinction values are based on NIR measurements, except in Juvela et al. (2002), where the *R* band was utilized. The results presented in Table 6 are all obtained using column densities derived with the LTE method, and assuming that the excitation temperatures for the CO isotopes are given by ^{12}CO, except in Juvela et al. (1997), where the optical depth of $C^{18}O$ was obtained from the ratio of $C^{18}O$ and ^{13}CO intensities.

6.3. Isotope abundance ratio $^{13}CO/C^{18}O$

We have examined the column density ratio of ^{13}CO and $C^{18}O$ isotopes as a function of extinction in the direction of globules B 335, B 133 and L 466. The results are shown in Fig. 11. This figure demonstrates the different behaviour of ^{13}CO and $C^{18}O$ as tracer of molecular material. Isotope-selective photodissociation together with the ^{13}CO fractionation are causing the increase of the ^{13}CO to $C^{18}O$ column density ratio at lower extinctions in Fig. 11 (cf. van Dishoeck 1988). The $N(^{13}CO)/N(C^{18}O)$ ratio decreases rapidly from a peak value of more than 20 at small extinctions to a value of ∼5.5, which is the terrestrial abundance ratio. The increase

of the $N(^{13}CO)/N(C^{18}O)$ ratio at low extinctions is striking in the case of B 335, and also clear in B 133, but is less prominent in L 466. This is mainly because there are no stars with $A_V < 0.4$ in B 133 and L 466. In B 133 and B 335 this ratio drops even below 5.5 at higher extinctions, which could be caused by the saturation of the ^{13}CO line.

6.4. $C^{18}O(J = 1 - 0)$ mapping of L 466

Our $C^{18}O(J = 1 - 0)$ mapping markedly reveals the clumpy structure of the globule with several density concentrations. In the densest core of the cloud there are signs of ring- or shell-like structure in the $C^{18}O$ map presented in Fig. 8. Fragmentation of a rotating cloud (Cha & Whitworth 2003) and depletion of CO isotopes on grains are effects that could cause this type of structure.

7. Conclusions

We have studied the $N(^{13}CO)$ vs. A_J and $N(C^{18}O)$ vs. A_J correlations in the direction of globules B 335, B 133 and L 466. For extinction determination we used background field stars with 2MASS JHK_s photometry available. The highest extinction value in each globule reaches up to $A_J \sim 2.0$–5.5 mag. We have used the 15-m SEST-telescope for observations of the selected positions in the $^{12}CO(J = 1 - 0)$ line, and the ^{13}CO and $C^{18}O$ $J = 1-0$ and $J = 2-1$ transitions. In agreement with our previous study, Paper I, the $N(^{13}CO)/A_J$ and $N(C^{18}O)/A_J$ ratios vary also in the case of globules from cloud to cloud, and appear to possibly reflect the level of star forming activity. In the same way, $N(^{13}CO)$ and $N(C^{18}O)$ vs. A_V and $N(H_2)$ vary from cloud to cloud. Caution should therefore be taken when using these ratios, since no justification was found for the use of one canonical $N(^{13}CO)/A_J$ or $N(C^{18}O)/A_J$ ratio in globules.

The $N(^{13}CO)/N(C^{18}O)$ ratio increases at lower extinctions at the edges of the clouds. This ^{13}CO abundance enhancement has the effect of making the $N(^{13}CO)$ vs. A_J slopes shallower.

Acknowledgements. We would like to thank the staff members of SEST telescope for their great hospitality during our observations. I am grateful to K. Mattila and J. Harju for their support and inspiration and also to A. Heikkilä for useful comments. We thank M. Juvela for providing the program used in the error analysis of CO column densities. This research was partially supported by the Academy of Finland (grant 101 1055), the Vilho, Yrjö, and Kalle Väisälä Foundation of the Finnish Academy of Science and Letters, the Finnish Cultural Fund and Alfred Kordelin Foundation. This publication makes use of data products from the Two Micron All Sky Survey, which is a joint project of the University of Massachusetts and the Infrared Processing and Analysis Center/California Institute of Technology, funded by the National Aeronautics and Space Administration and the National Science Foundation.

References

Alves, J., Lada, C. J., & Lada, E. A. 1999, ApJ, 515, 265
Bachiller, R., & Cernicharo, J. 1986, A&A, 166, 283
Bohlin, R. C., Savage, B. D., & Drake, J. F. 1978, ApJ, 224, 132
Bok, H. J. 1956, AJ, 61, 309
Booth, R. S., Delgado, G., Hagström, M., et al. 1989, A&A, 216, 315
Cardelli, J. A., Clayton, G. C., & Mathis, J. S. 1989, ApJ, 245, 345
Cha, S.-H., & Whitworth, A. P. 2003, MNRAS, 340, 91
Charnley, S. B., Dyson, J. E., Hartquist, T. W., & Williams, D. A. 1988, MNRAS, 231, 269
Clayton, G. C., & Mathis, J. S. 1988, ApJ, 327, 911
Dickman, R. L. 1978, ApJS, 37, 407
Dickman, R. L., & Herbst, W. 1990, ApJ, 357, 531
Elias, J. H. 1978a, ApJ, 224, 453
Elias, J. H. 1978b, ApJ, 224, 857
Encrenaz, P. J., Falgarone, E., & Lucas, R. 1975, A&A, 44, 73
Frerking, M. A., Langer, W. D., & Wilson, R. W. 1982, ApJ, 262, 590 FLW
Harjunpää, P., & Mattila, K. 1996, A&A, 305, 920, Paper I
Hayakawa, T., Mizuno, A., Onishi, T., et al. 1999, PASJ, 51, 919
Hayakawa, T., Cambrésy, L., Onishi, T., Mizuno, A., & Fukui, Y. 2001, PASJ, 53, 1109
Hotzel, S., Harju, J., Juvela, M., Mattila, K., & Haikala, L. K. 2002, A&A, 391, 275
Jolivette, P. L. 1993, Comp. Phys., 7, 208
Juvela, M., Lehtinen, K., Mattila, K., Lemke, D., & Haikala, L. 1997, A&A, 317, 898
Juvela, M., Mattila, K., Lehtinen, K., et al. 2002, A&A, 382, 583
Klebe, D., & Jones, T. J. 1990, AJ, 99, 638
Lada, C. J., Lada, E. A., Clemens, D. P., & Bally, J. 1994, ApJ, 429, 694
Lombardi, M., & Alves, J. 2001, A&A, 377, 1023
Mathis, J. S. 1990, ARA&A, 28, 37
Sanders, D. B., Solomon, P. M., & Scoville, N. Z. 1984, ApJ, 276, 182
van Dishoeck, E. F. 1988, ApJ, 334, 771
Vuong, M. H., Montmerle, T., Grosso, N., et al. 2003, A&A, 408, 581
Warin, S., Benayoun, J. J., & Viala, Y. P. 1996, A&A, 308, 535
Williams, D. A. 1985, QJRAS, 26, 463
Yun, J. L., & Clemens, D. P. 1990, ApJ, 365, L73
Yun, J. L., & Clemens, D. P. 1994, AJ, 108, 612
Yun, J. L., & Clemens, D. P. 1995, AJ, 109, 742
Yun, J. L. 1997, private communications

Online Material

Appendix B

Position	^{13}CO		C^{18}O	
	N_{LTE}	δN_{LTE}	N_{LTE}	δN_{LTE}
	10^{14} cm^{-2}		10^{14} cm^{-2}	
A4	39.2	2.4	2.4	0.2
A5	40.0	1.9	1.5	0.2
A6	34.9	2.3	7.6	0.6
A7	50.4	2.7	9.1	0.7
A8	41.4	2.5	8.4	0.7
A9	27.7	1.9	1.7	0.2
A10	21.9	1.6	2.2	0.2
A11	12.2	0.8	0.4	0.1
A12	53.1	3.0	13.4	1.0
A13	41.2	2.6	12.9	0.9
A14	49.3	2.7	8.3	0.6
B2	59.0	2.9	9.2	0.6
B3	71.8	3.1	20.7	1.1
B4	75.8	3.2	16.2	0.9
B5	60.9	2.5	6.8	0.4
B6	26.0	1.4	1.2	0.2
B7	66.2	3.2	6.2	0.5
B8	74.2	3.0	6.0	0.4
B9	84.7	4.7	16.1	0.9
B10	85.6	3.9	13.4	0.8
B11	45.3	2.7	2.8	0.3
B12	53.2	2.9	6.7	0.5
B13	80.3	3.6	10.0	0.6
B14	67.4	2.8	4.5	0.4
C1	52.6	1.5	5.3	0.2
C3	47.5	1.6	5.3	0.3
C4	57.4	1.7	7.9	0.4
C6	68.0	1.7	9.7	0.4
C9	75.3	2.0	14.0	0.6
C13	59.3	1.7	7.2	0.4
C14	49.7	1.9	6.3	0.4
C15	41.3	1.5	2.4	0.2
C18	50.0	1.8	5.9	0.4
C19	59.7	1.8	6.5	0.5
C20	37.6	1.2	3.3	0.2

Appendix C

Position	^{13}CO		C^{18}O	
	N	δN	N	δN
	10^{14} cm^{-2}		10^{14} cm^{-2}	
A4	32.2	2.8	1.8	0.2
A5	35.3	4.5	1.3	0.1
A6	28.6	3.1	6.1	0.6
A7	43.4	4.0	7.3	0.7
A8	35.9	3.9	6.7	0.7
A9	22.5	2.5	1.4	0.1
A10	17.8	2.0	1.8	0.2
A11	9.4	0.9	0.3	0.1
A12	45.1	4.3	10.9	1.2
A13	33.6	2.9	10.6	1.1
A14	40.7	4.0	6.5	0.6
B2	47.4	4.8	7.1	0.7
B3	61.2	6.5	17.2	1.9
B4	64.8	6.1	13.3	1.5
B5	51.3	5.8	5.5	0.5
B6	21.7	2.5	1.0	0.1
B7	52.6	4.3	4.7	0.4
B8	60.0	7.1	4.7	0.4
B9	70.1	5.8	12.6	1.3
B10	71.2	5.9	10.9	1.1
B11	36.4	4.4	2.2	0.2
B12	43.5	4.2	5.3	0.5
B13	62.7	5.4	7.6	0.8
B14	57.5	7.6	3.8	0.3
C1	47.2	6.0	4.5	0.5
C3	40.4	4.4	4.5	0.5
C4	50.5	6.1	6.6	0.7
C6	61.9	6.3	8.5	1.0
C9	65.6	5.4	11.9	1.5
C13	53.7	7.6	6.3	0.7
C14	42.7	4.6	5.2	0.6
C15	36.4	5.3	2.2	0.2
C18	42.6	5.7	4.8	0.5
C19	52.5	6.6	5.5	0.6
C20	32.7	4.7	2.7	0.3